Journal of Structural Biology xxx (xxxx) xxx–xxx

Contents lists available at ScienceDirect

Journal of Structural Biology

journal homepage: www.elsevier.com/locate/yjsbi

Improved applicability and robustness of fast cryo-electron tomography data acquisition

Fabian Eisenstein[a], Radostin Danev[b], Martin Pilhofer[a,*]

[a] Department of Biology, Institute of Molecular Biology & Biophysics, Eidgenössische Technische Hochschule Zürich, Otto-Stern-Weg 5, 8093 Zürich, Switzerland
[b] Graduate School of Medicine, The University of Tokyo, 7-3-1 Hongo, Bunkyo-ku, Tokyo 113-0033, Japan

ARTICLE INFO

Keywords:
Cryo-electron tomography
Electron cryotomography
Cryo-EM
Tilt series
Data acquisition
Throughput
K2
K3
Calibration

ABSTRACT

The power of cryo-electron tomography (cryoET) lies in its capability to characterize macromolecules in their cellular context. Structure determination by cryoET, however, is time-consuming compared to single particle approaches. A recent study reported significant acceleration of data acquisition by a fast-incremental single-exposure (FISE) tilt series scheme.

Here we improved the method and evaluated its efficiency and performance. We show that (1) FISE combined with the latest generation of direct electron detectors speeds up collection considerably, (2) previous generation (pre-2017) double-tilt axis Titan Krios holders are also suitable for FISE data acquisition, (3) x, y and z-specimen shifts can be compensated for, and (4) FISE tilt series data can generate averages of sub-nanometer resolution.

These advances will allow for a widespread adoption of cryoET for high-throughput *in situ* studies and high-resolution structure determination across different biological research disciplines.

1. Introduction

Cryo-electron tomography (cryoET) and subtomogram averaging are emerging as a powerful structure determination alternative to single particle cryo-electron microscopy (SPA). In contrast to SPA, cryoET offers the possibility of determining structures of macromolecular complexes in their biological context (Briggs, 2013). New methods and software packages are being developed to overcome barriers that currently prevent the determination of structures at a quality that is comparable to SPA (Danev et al., 2019; Schur, 2019). While both, cryoET and SPA, rely on the collection of data from thousands of copies of identical proteins to improve the low signal-to-noise ratio that is inherent to cryo-electron microscopy of biological samples, SPA data collection yields many-fold more particles given the same collection time. In addition, high-resolution cryoET projects usually employ special tilt series acquisition schemes that further slow down data collection (Hagen et al., 2017). Especially in cases of only a few target copies per field of view, many days of microscope time are required to obtain sufficient numbers of subvolumes for subtomogram averaging.

The Titan Krios cryo-transmission electron microscope (Thermo Scientific) is currently the prevalent high-end model used for cryoET. Most of the installed instruments are equipped with a dual-tilt axis (DT) holder that is capable of rotating the specimen by 90° inside the column to facilitate dual-axis tomography. A recent publication reported a new single-tilt axis (ST) holder for the Titan Krios (installed in 2017), whose improved mechanical performance allows for collection of tilt series in a matter of minutes instead of hours (Chreifi et al., 2019). These time savings result from omitting time-intensive tracking, autofocusing, tilt-backlash correction and settling steps, which were previously deemed essential for the collection of high-resolution data (Hagen et al., 2017). The introduced 'fast-incremental single-exposure' (FISE) method additionally saves time by acquiring a complete tilt series in a single long exposure. In this procedure, the camera is continuously acquiring and sample exposure is controlled by blanking of the electron beam. The beam is blanked while the stage is tilting and unblanked when the stage is stationary at each tilt angle of the tilt scheme. This method eliminates camera start-up times of several seconds per tilt exposure, which were needed during conventional tilt series acquisition (Chreifi et al., 2019).

Here, we address several questions that had to be answered before FISE tilt series acquisition can be widely adopted: (1) The next generation of direct electron detectors (here the Gatan K3 camera) was able to further accelerate tilt series acquisition by essentially eliminating processing time, which previously disabled the microscope control interface (SerialEM) for several minutes. (2) Interestingly, we found that the conventional DT holder was also suitable for FISE data acquisition. (3) We established that specimen shifts during tilting can be calibrated

Abbreviations: FISE, fast-incremental single-exposure; ST, single-tilt axis; DT, dual-tilt axis

* Corresponding author.
E-mail address: pilhofer@biol.ethz.ch (M. Pilhofer).

https://doi.org/10.1016/j.jsb.2019.08.006
Received 5 July 2019; Received in revised form 12 August 2019; Accepted 14 August 2019
1047-8477/ © 2019 The Author(s). Published by Elsevier Inc. This is an open access article under the CC BY-NC-ND license (http://creativecommons.org/licenses/BY-NC-ND/4.0/).

Please cite this article as: Fabian Eisenstein, Radostin Danev and Martin Pilhofer, Journal of Structural Biology, https://doi.org/10.1016/j.jsb.2019.08.006

and compensated for, by applying tilt angle dependent image shifts and defocus. (4) Finally, we showed that the data quality of FISE tilt series was sufficient to achieve subnanometer resolution by subtomogram averaging.

2. Results and discussion

In order to ensure reproducibility and wide applicability, we performed FISE experiments on three Titan Krios transmission electron microscopes. Two of the instruments were equipped with a ST holder and a Gatan K3 direct electron detector, hereafter referred to as Titan Krios [ST/K3] and one was equipped with a previous generation DT holder and a Gatan K2 direct electron detector, hereafter Titan Krios [DT/K2] (Table S1).

2.1. FISE tilt series acquisition using a K3 direct electron detector

FISE acquisition produces a single movie containing hundreds of frames which has to be processed and saved by the camera hardware after each tilt series. Using the Gatan K2 direct electron detector in Counting mode, this processing time is in the order of minutes and disables the microscope control interface (SerialEM), contributing up to 50% of the total acquisition time (Chreifi et al., 2019). In addition to providing an approximately 65% larger field of view (K2: 3'838 × 3'710 pixels; K3: 5'760 × 4'092 pixels), the Gatan K3 direct electron detector is superior to the K2 in two major ways: (1) its higher readout speed allows for a higher dose rate and hence, for shorter exposure times per frame and per tilt, and (2) its improved processing speed facilitates a faster output of frames and less delay to regain microscope control through the interface after an exposure. We compared the performance of FISE tilt series acquisition on Titan Krios [DT/K2] in Counting mode with Titan Krios [ST/K3] in Super-Resolution mode with hardware binning by a factor of two (Table 1, Table S2). Regardless of the change in terminology, both camera modes represent the same super-resolution electron counting followed by simple 2x pixel binning. On Titan Krios [DT/K2] a full 120° dose-symmetric tilt series with 3° increments could be collected in ~5.7 min. The measured times on Titan Krios [ST/K3] confirmed that the new generation of Gatan direct electron detectors was able to essentially eliminate the processing time that blocks the microscope control interface (SerialEM) after long exposures. While the difference between 'set Record time' and the actual 'camera Record time' was over two minutes on the K2, it was reduced to four seconds on the K3. Full 120° tilt series with 3° increments could be collected in 2.2 min on Titan Krios [ST/K3] and automated serial acquisition of tilt series required less than 5 min per preselected target, allowing for a throughput of 10–15 FISE tilt series per hour. On a Titan Krios [DT/K2], 6–7 FISE tilt series per hour should be achievable. Furthermore, the latest SerialEM version 3.7 beta12 (or higher) can discard frames with a mean count below a defined threshold (blanked frames) on the fly, which results in faster processing and smaller file sizes compared to previous versions.

Table 1
K3 camera eliminates long processing times. Time measurements of FISE −60° to +60° tilt series with 3° increments on Titan Krios [DT/K2] and Titan Krios [ST/K3].

Instrument	Tilt scheme	Unblank time[a]	Prep time[b]	Set Rec time[c]	Cam Rec time[d]	Total time[e]
[ST/K3]	unidirectional	1 s	98 s	91 s	95 s	201 s
[DT/K2]	unidirectional	1 s	136 s	117 s	253 s	399 s
[ST/K3]	dose-symmetric	1 s	101 s	130 s	134 s	243 s
[DT/K2]	dose-symmetric	1 s	134 s	185 s	339 s	484 s

[a] Time the sample is exposed per tilt.
[b] Time taken to refine eucentricity and autofocus.
[c] Exposure time set for Record in SerialEM. Variations are due to the slower tilt speed on Titan Krios [DT/K2]. In all cases, the default tilt speed of the stage was not altered.
[d] Time from start of acquisition until regain of microscope control.
[e] Total run time of the tilt series including resetting the microscope state.

2.2. Performance of single-tilt axis holder and dual-tilt axis holder

A prototype of the new Titan Krios ST holder was recently shown to be eucentric enough for the collection of fast-incremental tilt series without the need for additional tracking images (Chreifi et al., 2019). To confirm that this behavior was reproducible across Titan Krios instruments equipped with the new ST holder, we recorded the x- and y-shift (parallel and perpendicular to the tilt axis, respectively) of a specimen throughout the tilt series on a Titan Krios [ST/K3]. During the collection of dose-symmetric FISE tilt series with an increment of 3° and a range from −60° to +60°, we observed specimen shifts perpendicular to the tilt axis of ± 300–600 nm (Fig. 1A), which is consistent with the previously published results that accounted for a range of −51° to +51° (Chreifi et al., 2019). Specimen shifts observed parallel to the tilt axis (x-shift) were negligible (Fig. 1B).

In order to quantify the improvement of the new ST holder over the previous generation Titan Krios DT holder, we used the same FISE tilting scheme and recorded tilt series on a Titan Krios [DT/K2]. Interestingly, the observed x- and y-shifts in the tilt series (Fig. 1C/D) were comparable to those obtained from the ST holder, suggesting that the performance gain by using the ST holder is not substantial. The DT holder, however, showed significantly larger specimen shifts occurring reproducibly upon change of tilt direction (at 0° in case of dose-symmetric tilt scheme). As a result of this systematic mechanical error, the specimen was shifted by ~200 nm at negative tilt angles relative to positive tilt angles (arrowhead in Fig. 1C). During state-of-the-art dose-symmetric acquisition schemes, this effect is minimized by taking additional time to approach all tilt angles from the same direction (Hagen et al., 2017). To maximize speed, such backlash-compensation was not performed here. The specimen shift profiles throughout the tilt series showed a certain degree of reproducibility for both holders, which suggested that calibrations may be used to compensate for specimen shifts.

2.3. Calibrated image shift compensation of specimen shifts

Previous specimen shift analyses showed partial reproducibility of stage errors throughout a dose-symmetric FISE tilt series (Chreifi et al., 2019), suggesting the possibility of using image shifts for compensation of specimen shifts during acquisition. Calibrated image shift compensation of tilt-induced specimen shifts has been used in earlier efforts to automate tilt series collection and compensate for errors in stage eucentricity and offset between the optical axis and the tilt axis (Ziese et al., 2002). Using a model for stage geometry and on the fly-measured specimen shifts allowed for further refinements of local parameters, which improved the robustness of stage movement predictions (Zheng et al., 2004).

To minimize specimen shifts caused by the offset between the optical axis and the tilt axis, we used the SerialEM image shift correction that is applied after analysis of the average lateral displacement of several runs of the fine eucentricity routine. Furthermore, to ensure eucentricity for every target, the fine eucentricity routine was run immediately before the start of every FISE tilt series collection. Currently, specimen shift cannot be measured on the fly within a FISE tilt series, because frames are saved by SerialEM only after the completion of the single long exposure. Hence, corrections have to rely entirely on precalibrated image shifts assuming a consistent specimen geometry and stage behavior between targets. To test the feasibility of this approach, we collected a tilt series with short single exposures per tilt angle and recorded the specimen shifts throughout a dose-symmetric tilt scheme. The collection and processing of this calibration tilt series took about

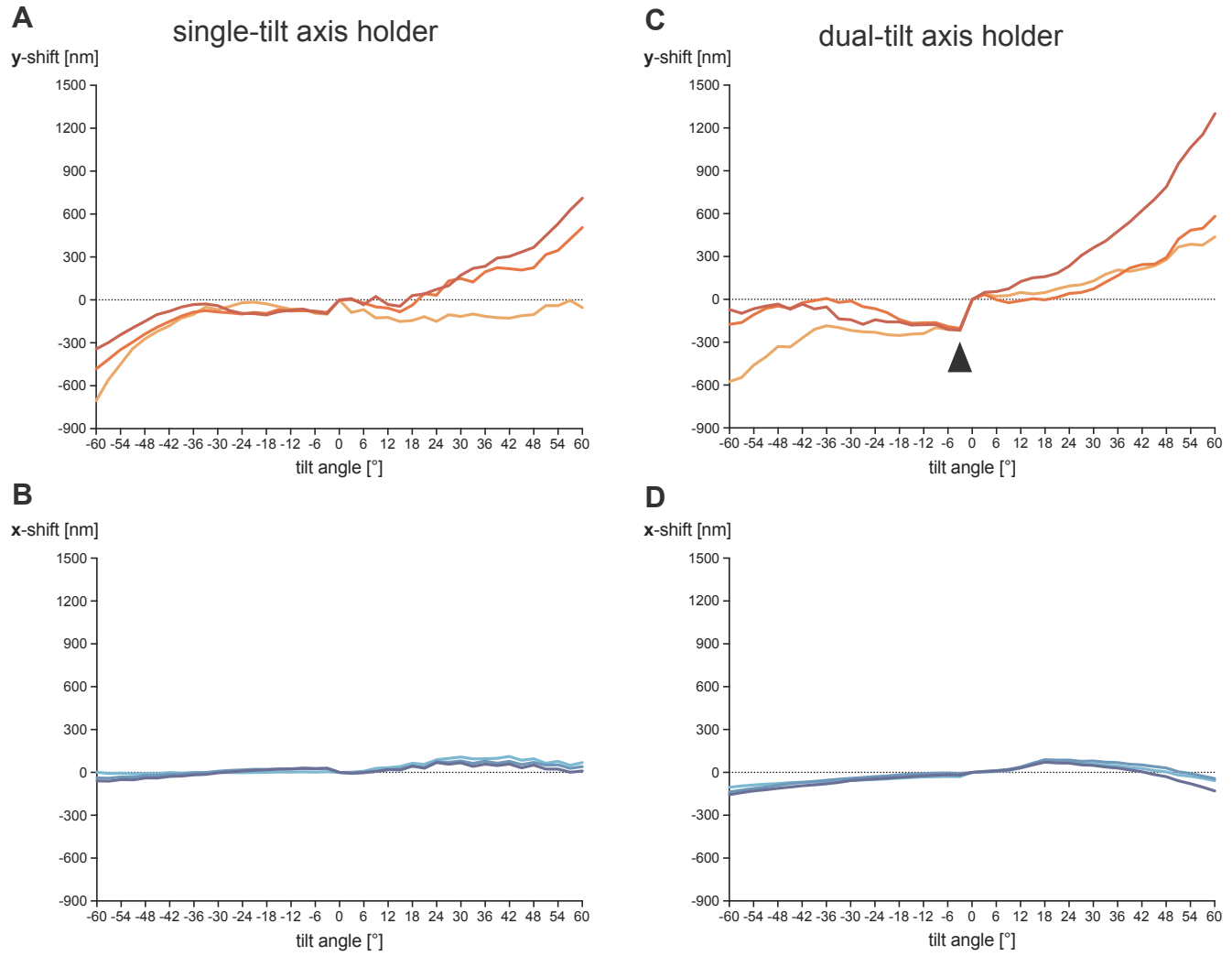

Fig. 1. Performance increase of ST holder compared to DT holder is marginal. Representative examples of specimen shift throughout a FISE dose-symmetric 3° increment tilt series recorded using a single-tilt (ST) axis holder (A/B) or a dual-tilt (DT) axis holder (C/D). The tilt axis in both cases is approximately parallel to the x-axis. Overall, specimen shifts are comparable between both holders and x-shift is negligible compared to y-shift. The DT holder shows larger systematic shift upon reversal of tilt direction (arrowhead).

six minutes on a Titan Krios [ST/K3]. Subsequently, we applied compensating image shifts during the collection of a FISE tilt series. The resulting specimen shifts were significantly reduced, showing a total shift of the target within ± 100 nm (Fig. 2A/B, Movies S1 and S2), which is less than 10% of the detector area at 2.7 Å/pixel on a K3.

Stability and reproducibility of the calibrated image shifts were tested by collection of FISE tilt series at a distance of up to two grid squares from the position where the calibration tilt series was acquired (Fig. 2C/D). The compensated specimen shifts could be kept below 200 nm on the calibration square (red) and below 500 nm at a distance of two squares from the calibration position (blue). The reference tilt series without compensation showed maximum specimen shifts between 770 nm and 1250 nm (Fig. 2D, grey). These results suggest that the quality of compensation is dependent on the local specimen support geometry. To evaluate at which tilt angles most data was lost, we calculated the loss of data, taking into account the gain of field of view perpendicular to the tilt axis at higher tilt angles and the compression of the specimen projection (Fig. S1A). As expected, the maximum loss of data occurred at high tilt angles for uncompensated tilt series and at lower tilt angles for image shift-compensated tilt series (Fig. S1B). Due to the gain of field of view, lower tilt angles are more sensitive to specimen shift and hence small inaccuracies in calibrations and local specimen variability.

Nonetheless, image shift compensation should allow for the collection of tens to hundreds of FISE tilt series with a single set of calibrated image shifts. Similar results were obtained for a Titan Krios [DT/K2] (Fig. S2).

Next, we assessed the calibration robustness on a real sample with two to seven targets per square on eleven squares total. After recording a single set of calibrated image shifts in the central square (Fig. S3), we collected 47 FISE tilt series of metamorphosis-associated contractile structures (MACs) (Shikuma et al., 2014) in less than four hours on a Titan Krios [ST/K3]. The maximum specimen shifts varied significantly between tilt series (Fig. 2E). In the best tilt series the specimen shifts were less than 130 nm while in the worst tilt series they were over 650 nm. The biggest shifts, however, occurred usually at high tilts (blue crosses in Fig. 2E). Considering the increase in visible specimen area perpendicular to the tilt axis at high tilt angles (doubled at 60°), the maximum loss of data was less than 40% of the specimen area at 0° in most cases (Fig. S1C) with the worst case showing a 70% loss of data for one tilt angle (see Movie S3 for the tilt series with largest loss of data, indicated by arrowhead in Fig. 2E). Overall, no micrographs had to be discarded in any of the tilt series. Furthermore, average lateral displacement measured by the fine eucentricity routine in SerialEM was −0.03 µm with a standard deviation of 0.13 µm excluding one outlier. This showed good compensation of the tilt axis offset from the optical

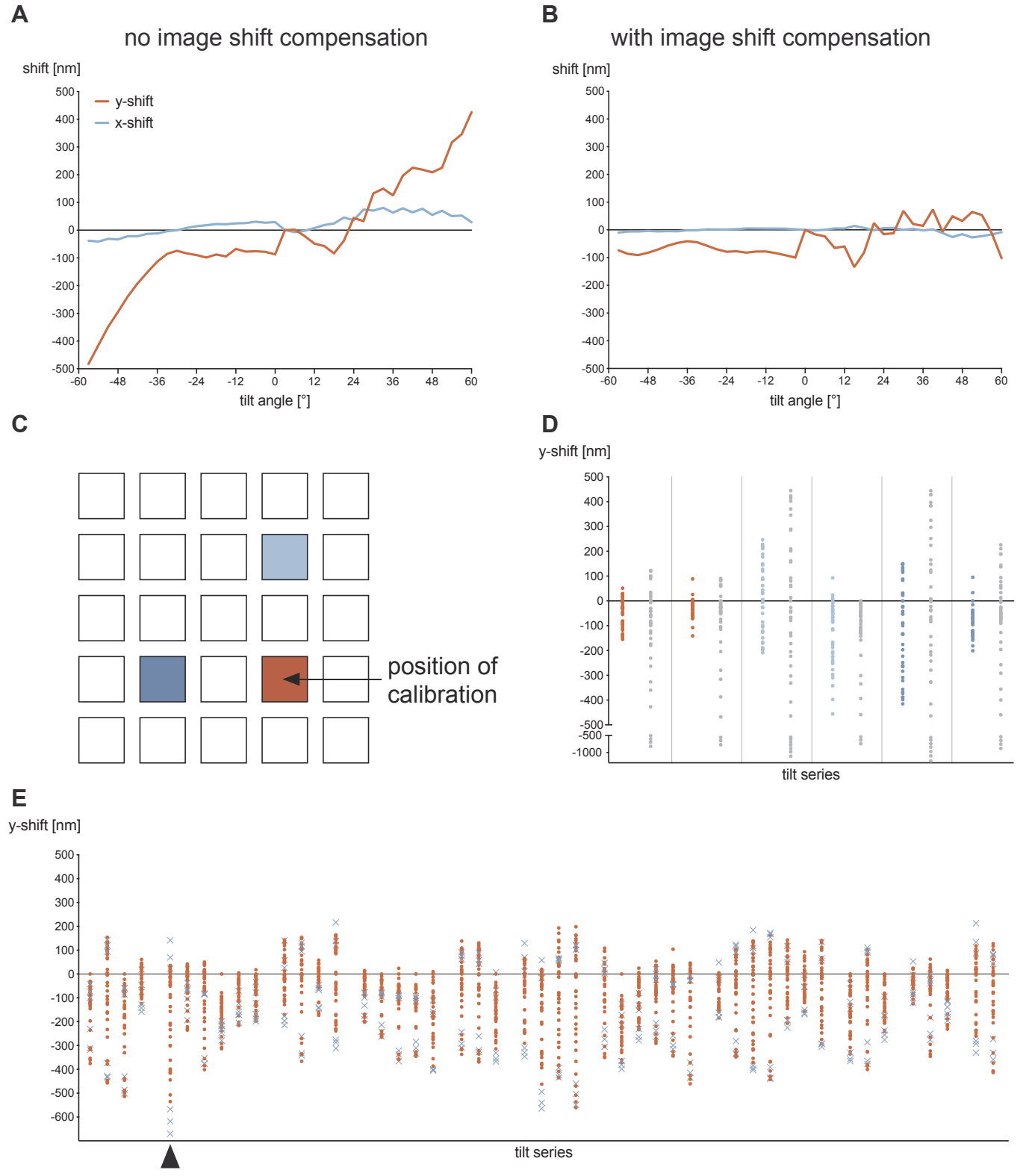

Fig. 2. Image shift compensation can be used to minimize specimen shifts. A/B: Specimen shift throughout a FISE dose-symmetric 3° increment tilt series recorded without application of compensating image shifts (A) and with application of compensating image shifts (B) recorded on a Titan Krios [ST/K3]. Image shifts effectively compensate specimen shifts, especially at large tilt angles. C/D: A single calibration tilt series can be used to compensate specimen shifts for multiple grid squares. The schematic (C) shows squares of a Quantifoil Cu 200 R2/2 grid and refers to the relative positions of tilt series that were collected with (colored) and without (grey) compensating image shifts (D). Shown are specimen shifts perpendicular to the tilt axis (y-shift) within full tilt series. E: Y-shifts of 47 tilt series collected in less than four hours on eleven different squares (Fig. S3) using a single calibration tilt series and a Titan Krios [ST/K3]. Blue crosses mark tilt angles higher than ± 51°. The arrowhead indicates the worst tilt series that is also shown in Movie S3. Tilt series are grouped by squares. No micrographs had to be discarded due to the loss of target.

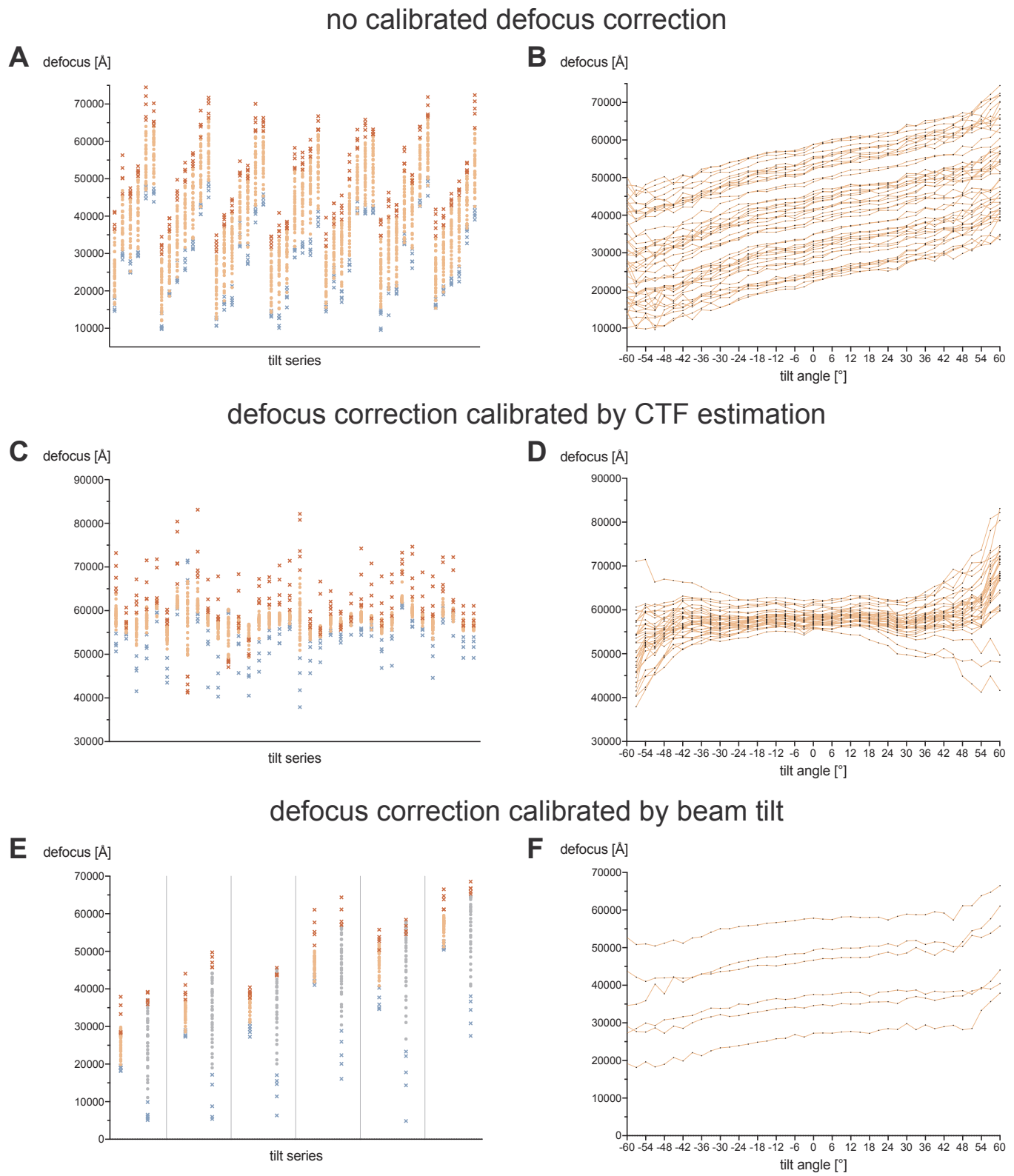

Fig. 3. Z-shifts can be partially compensated by pre-calibrated defocus offsets. Estimated defocus of motion-corrected micrographs within individual FISE dose-symmetric tilt series (A/C/E) and per tilt angle (B/D/F). Red crosses mark tilt angles higher than 45° and blues crosses mark tilt angles lower than −45°. Data was collected on a Titan Krios [ST/K3]. A/B: 47 tilt series with a cycling target defocus between 2 and 5 µm and a step size of 0.5 µm. Defocus change is over 2 µm per tilt series (A) and shows approximately linear dependence on tilt angle (B). C/D: 36 tilt series with a target defocus of 5 µm and tilt angle-dependent defocus correction determined by CTF analysis of a calibration tilt series. Calibrations can compensate for defocus change in an angular range of ± 45°. E/F: 9 tilt series with a cycling target defocus between 2.5 and 5 µm and tilt angle-dependent defocus correction determined by beam tilt defocus measurement at four tilts of a calibration tilt series. Grey tilt series in (E) were taken at the same stage position without applying the defocus correction. Calibrations can reduce defocus change within ~1 µm at an angular range of ± 45°.

axis and further consolidated that fluctuations in specimen shifts depend primarily on specimen geometry. Overall, these results showed that the FISE tilt series acquisition is usable for the collection of large datasets with minimal extra effort and results in vast time savings.

2.4. Z-shift compensation by defocus changes

Having addressed specimen movement in the x- and y-directions, we set out to investigate specimen movement along the z-axis. By Contrast Transfer Function (CTF) estimation, we determined the defocus values of individual tilts from the 47 tilt series that were collected on MACs. The changes in z-height throughout the tilt series remained in the order of a few microns (Fig. 3A). We found that the z-shift behaved predictably with an approximately linear dependence on the tilt angle (Fig. 3B, also seen by Chreifi et al., 2019).

To compensate for the z-shift, we determined the slope of the defocus over the tilt angle for one tilt series using CTF estimation by gctf (Zhang, 2016) and applied a tilt-dependent defocus shift (as described previously by Ziese et al., 2002) to 36 tilt series collected on the same specimen. The resulting defocus spread was less than 1 μm for tilt angles between −45° and + 45° in over 90% of the collected tilt series (Fig. 3C/D).

Using currently available software, it is not straightforward to accurately and reliably estimate the CTF of a high tilt angle micrograph on the fly. Hence, we used the beam-tilt routine of SerialEM to measure the defocus (Koster et al., 1987) at four tilt angles to approximate the defocus slope during the collection of the image shift calibrations. Applying a compensating defocus change to FISE tilt series showed a considerable improvement of defocus spread (Fig. 3E and F) to almost the same level of accuracy as obtained by defocus slope determination by CTF estimation using gctf.

The achieved z-shift compensation by defocus calibrations was adequate for most targets, but not sufficient when precise and consistent defocus is required, like for the use of a Volta phase plate (Khoshouei et al., 2017).

2.5. Data quality and subtomogram averaging

For the FISE approach to be widely adopted, it must be able to provide high-resolution data for subtomogram averaging. Previously, data quality of FISE tilt series was analyzed by visual inspection and cellular subtomogram averaging of methyl-accepting chemotaxis protein arrays to an estimated resolution better than 2.5 nm (Chreifi et al., 2019). An increasing number of studies, however, report subtomogram averaging projects that result in structures at sub-nanometer resolutions (Schur et al., 2016; Mattei et al., 2018; Hutchings et al., 2018). Hence, we used the *E.* coli 70S ribosome as a benchmarking sample to test the capabilities of the FISE method for subtomogram averaging. We recorded a dataset of twelve FISE dose-symmetric tilt series on a Titan Krios [ST/K3] in less than 50 min to obtain a subtomogram average (Fig. 4A). 11'251 particles were picked by template matching in emClarity (Himes and Zhang, 2018) and subtomogram averaging of 9'923 final subvolumes yielded a map at a subnanometer resolution (Fig. 4B), which is supported by visible secondary structure features like rod-shaped alpha-helices and ribosomal RNA double helices (Fig. 4C). These results demonstrate that drift settling and precise autofocus, which are the most time-consuming components of conventional tilt series acquisition schemes, are not resolution-limiting for most tomography specimens and therefore can be omitted for considerable throughput benefits.

3. Conclusions

Many software improvements over the last decade made robust acquisition of tilt series possible even at small pixel sizes. Omitting important steps of current acquisition schemes including tracking, drift settling, backlash correction and autofocus, might seem like a step backwards when it comes to data quality. Here we showed, however, that the combination of recent advances in hardware, such as fast direct electron detectors, with basic calibrations enables robust FISE data acquisition even on previous generation Titan Krios holders. Significant loss of field of view can be avoided and data quality is sufficient for most cellular and *in vitro* structural studies. The FISE acquisition scheme drastically reduces data collection times and is capable of producing subtomogram averages at sub-nanometer resolution. Cellular tomography, in particular, will experience major benefits from the FISE method where it will remove the throughput barrier for *in situ* studies of low abundance targets within cellular volumes.

Future enhancements of data acquisition software might improve the robustness of the technique through on the fly analysis of output frames for specimen shift and defocus, in order to refine the predetermined calibration values. With the increased throughput in data collection, other steps of the pipeline will become time limiting. Efforts should be continued to explore new methods for the automation of target selection on the grid (Schorb et al., 2019), the alignment of tilt series, the segmentation of tomograms, and the picking of subtomograms by template matching and template-free structural pattern mining (Himes and Zhang, 2018; Chen et al., 2017; Hrabe et al., 2012; Castaño-Díez et al., 2012; Winkler, 2007; Xu et al., 2019). Together, these developments will make cryoET a high-throughput method that is capable of analyzing the spatial and temporal distribution of macromolecules as well as their structure *in situ*.

4. Materials and methods

4.1. MAC sample preparation

MACs were purified as described previously (Shikuma et al., 2014). Briefly, *Pseudoalteromonas luteoviolacea* was grown in 50 ml Marine Broth (MB) media in 250 ml flasks at 30 °C for 5–6 h. Cells were centrifuged for 30 min at 7'000*g* and 4 °C and resuspended in 5 ml cold extraction buffer (20 mM Tris, pH 7.5, 1 M NaCl). Cultures were centrifuged for 30 min at 4'000 × *g* and 4 °C and the supernatant (SN) was isolated. 1% Triton X-100 was added to the SN and incubated at 20 °C for 15 min. The SN was centrifuged for 30 min at 7'000 × *g* and 4 °C. The pellet was resuspended in about 50 μL of residual buffer and mixed with Protein A-conjugated 5-nm colloidal gold (Cytodiagnostics Inc.) before plunge freezing. Plunge freezing was performed according to Weiss et al., 2017. 4 μL of sample was applied to glow-discharged EM grids (R2/1 copper, Quantifoil), blotted twice from the back for 3.5 s and vitrified in liquid ethane–propane (37 v/v% ethane) using a Vitrobot Mark IV (Thermo Scientific).

4.2. 70S ribosome sample preparation

500 ml of *E. coli* DH5alpha were grown in Luria-Bertani broth (LB) to an absorbance at 600 nm (OD_{600}) of about 0.6 and harvested by centrifugation at 6'500*g* for 15 min at 4 °C. Cells were resuspended in 3 ml lysis buffer (20 mM Tris-HCl pH 7.5, 100 mM KOAc, 10 mM $Mg(OAc)_2$, 0.5 mM $CaCl_2$, 1 mM Dithiothreitol (DTT), 30 μg/mL chloramphenicol, 100 μg/mL Lysozyme, 30 μg/mL DNAse I) incubated at 20 °C for 30 min and frozen at −20 °C. The lysate was thawed and cell debris was removed by centrifugation at 20'400*g* and 4 °C for 30 min. Cleared lysate was layered on top of 400 μL sucrose cushion [20 mM Tris-HCl pH 7.5, 100 mM KOAc, 10 mM $Mg(OAc)_2$, 1 mM DTT, 30 μg/mL chloramphenicol, 750 mM sucrose] and spun at 417'200 × g and 4 °C for 1 h. The pellet was washed twice with 50 μL resuspension buffer [20 mM Tris-HCl pH 7.5, 100 mM KOAc, 10 mM $Mg(OAc)_2$, 1 mM DTT, 30 μg/mL chloramphenicol] and resuspended in 150 μL resuspension buffer. Before plunge freezing the sample was diluted 1:50 and 10 nm colloidal gold fiducials (Aurion BSA tracer 10 nm) were added. 4 μL of sample was applied to glow-discharged EM grids (Cu 200 R2/2,

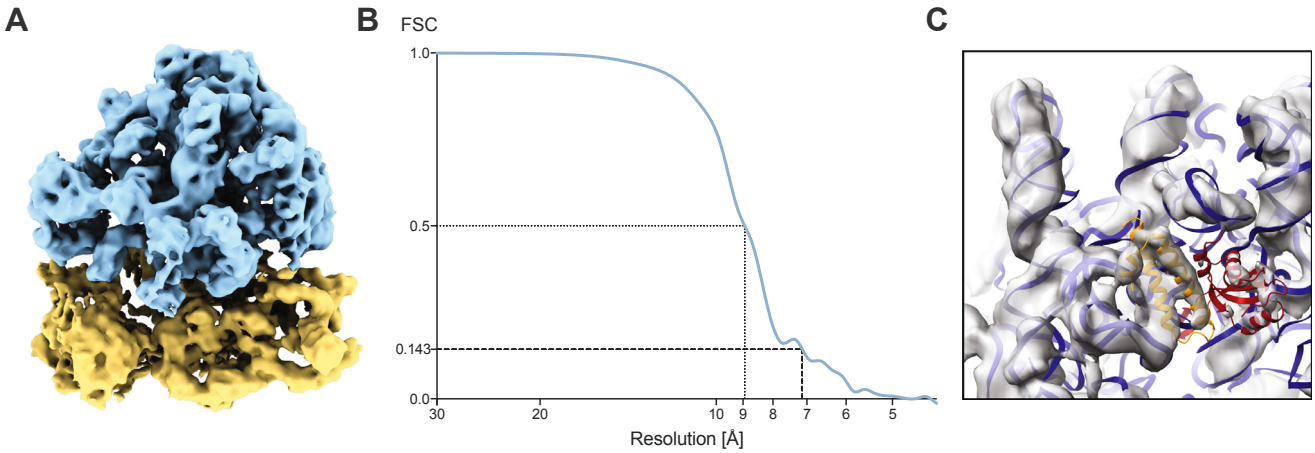

Fig. 4. FISE tilt series acquisition can generate a sub-nanometer average. A: Subtomogram average of the *E. coli* 70S ribosome obtained from FISE tilt series. Blue: large subunit, yellow: small subunit. B: Gold standard FSC curve calculated using emClarity. C: Subtomogram average fitted with the atomic model of a 70S ribosome (PDB 5MDZ). Note the visibility of secondary structure features like rod-shaped alpha helices (yellow) and ribosomal RNA double helices (blue).

Quantifoil), blotted for 3 s and vitrified in liquid ethane using a Vitrobot Mark IV (Thermo Scientific).

4.3. Tilt series acquisition and data processing

CryoET data were collected on three Titan Krios (Thermo Scientific) transmission electron microscopes equipped with a Quantum LS imaging filter (Gatan, slit with 20 eV), single-tilt axis holder or dual-tilt axis holder and K3 or K2 direct electron detector (Gatan) (Table S1). Tilt series were acquired with the software SerialEM (Mastronarde, 2005, Schorb et al., 2019) using the FrameSeriesFromVar command to setup a FISE dose-symmetric tilt scheme with per tilt applied image shifts and defocus changes. The angular range was -60° to $+60^{\circ}$ and the angular increment was 3° unless specified otherwise. The total electron dose was between 120 and 150 electrons per $Å^2$ and the pixel size at specimen level was 2.1 Å for the 70S ribosome data set and 2.7 Å or 2.8 Å for other data sets from Titan Krios [ST/K3] and Titan Krios [DT/K2], respectively. Tilt series were saved as single stack of frames and subsequently separated using a custom python script. Frames were aligned with IMOD (Mastronarde, 1997), defocus was estimated using gctf (Zhang, 2016) and micrographs were exposure-filtered (Grant and Grigorieff, 2015). Specimen shifts were estimated using the IMOD function tiltxcorr, tilt series were aligned using gold fiducials, CTF was corrected using IMOD and three-dimensional reconstructions were calculated by weighted back projection using IMOD.

4.4. 70S ribosome subtomogram averaging

Tilt series were aligned as described above, but CTF estimation and correction as well as exposure-filtering were performed using emClarity (Himes and Zhang, 2018). 11'251 particles were picked from twelve tomograms by emClarity template matching using EMD-6311 as template. Particle extraction, alignment and averaging was performed using the emClarity pipeline. Using template matching alignment parameters, particles were aligned 4×4-binned for three iterations. Duplicate particles were removed and alignment was continued for three iterations using 2×2-binned tomograms, before seven iterations of alignment of un-binned particles. Particles were classified into four classes according to the presence of the 40S subunit using PCA and k-means clustering in emClarity. One class representing 50S subunits was excluded and the remaining 9'923 particles were aligned for one more iteration. The gold standard Fourier shell correlation curve was calculated by emClarity (Fig. 4B).

4.5. Data deposition

Subtomogram averages were deposited in the Electron Microscopy Data Bank (EMDB accession code: EMD-10211), and tilt series in the Electron Microscopy Public Image Archive (EMPIAR accession code: EMPIAR-10304).

SerialEM scripts are available at The SerialEM Script Repository (https://serialemscripts.nexperion.net/) and a python script extracting tilt images from a FISE frame stack is available on https://github.com/feisenstein/FISE.

Declaration of Competing Interest

The authors declare that they have no known competing financial interests or personal relationships that could have appeared to influence the work reported in this paper.

Acknowledgements

We thank Simone Mattei for discussions on subtomogram averaging, David Mastronarde for the implementation of special SerialEM scripting commands, Grant Jensen for discussions on fast-tilt series acquisition, Masahide Kikkawa for providing lab space/chemicals for the ribosome preparation, Benjamin Himes for help and discussions on subtomogram averaging using emClarity, Katarzyna Radomska for advice on statistics and plotting, and Yoshiyuki Fukuda for reagents and discussions. ScopeM is acknowledged for instrument access at ETH Zürich. Ariane Briegel and Rebecca Dillard are acknowledged for the possibility of a test measurement at NeCEN. Work in the Pilhofer Lab was supported by ETH Zürich, the NOMIS foundation, the Swiss National Science Foundation (164092, 179255, 170808), and the European Research Council (679209). Radostin Danev was supported by grants from the Japan Society for the Promotion of Science (JSPS) KAKENHI #18H06043 and the Japan Science and Technology Agency (JST) PRESTO #18069571. FE received an exchange fellowship from the Japan Society for the Promotion of Science (JSPS).

Appendix A. Supplementary data

Supplementary data to this article can be found online at https://doi.org/10.1016/j.jsb.2019.08.006.

ARTICLE IN PRESS

References

Briggs, J.A., 2013. Structural biology in situ—the potential of subtomogram averaging. Curr. Opin. Struct. Biol. 23, 261–267. https://doi.org/10.1016/j.sbi.2013.02.003.

Castaño-Díez, D., Kudryashev, M., Arheit, M., Stahlberg, H., 2012. Dynamo: a flexible, user-friendly development tool for subtomogram averaging of cryo-EM data in high-performance computing environments. J. Struct. Biol. 178, 139–151. https://doi.org/10.1016/j.jsb.2011.12.017.

Chen, M., Dai, W., Sun, S.Y., Jonasch, D., He, C.Y., Schmid, M.F., Chiu, W., Ludtke, S.J., 2017. Convolutional neural networks for automated annotation of cellular cryo-electron tomograms. Nat. Methods 14, 983–985. https://doi.org/10.1038/nmeth.4405.

Chreifi, G., Chen, S., Metskas, L.A., Kaplan, M., Jensen, G.J., 2019. Rapid tilt-series acquisition for electron cryotomography. J. Struct. Biol. 205, 163–169. https://doi.org/10.1016/j.jsb.2018.12.008.

Danev, R., Yanagisawa, H., Kikkawa, M., 2019. Cryo-electron microscopy methodology: current aspects and future directions. Trends Biochem. Sci. https://doi.org/10.1016/j.tibs.2019.04.008.

Grant, T., Grigorieff, N., 2015. Measuring the optimal exposure for single particle cryo-EM using a 2.6 Å reconstruction of rotavirus VP6. eLife. https://doi.org/10.7554/eLife.06980.

Hagen, W.J.H., Wan, W., Briggs, J.A., 2017. Implementation of a cryo-electron tomography tilt-scheme optimized for high resolution subtomogram averaging. J. Struct. Biol. 197, 191–198. https://doi.org/10.1016/j.jsb.2016.06.007.

Himes, B.A., Zhang, P., 2018. emClarity: software for high-resolution cryo-electron tomography and subtomogram averaging. Nat. Methods 15, 955–961. https://doi.org/10.1038/s41592-018-0167-z.

Hutchings, J., Stancheva, V., Miller, E.A., Zanetti, G., 2018. Subtomogram averaging of COPII assemblies reveals how coat organization dictates membrane shape. Nature Commun. 9. https://doi.org/10.1038/s41467-018-06577-4.

Hrabe, T., Chen, Y., Pfeffer, S., Cuellar, L.K., Mangold, A.V., Förster, F., 2012. PyTom: a python-based toolbox for localization of macromolecules in cryo-electron tomograms and subtomogram analysis. J. Struct. Biol. 178, 177–188. https://doi.org/10.1016/j.jsb.2011.12.003.

Khoshouei, M., Pfeffer, S., Baumeister, W., Förster, F., Danev, R., 2017. Subtomogram analysis using the Volta phase plate. J. Struct. Biol. 197, 94–101. https://doi.org/10.1016/j.jsb.2016.05.009.

Koster, A.J., Van den Bos, A., van der Mast, K.D., 1987. An autofocus method for a TEM. Ultramicroscopy 21, 209–222. https://doi.org/10.1016/0304-3991(87)90146-X.

Mastronarde, D.N., 1997. Dual-axis tomography: an approach with alignment methods that preserve resolution. J. Struct. Biol. 120 (3), 343–352. https://doi.org/10.1006/jsbi.1997.3919.

Mastronarde, D.N., 2005. Automated electron microscope tomography using robust prediction of specimen movements. J. Struct. Biol. 152, 36–51. https://doi.org/10.1016/j.jsb.2005.07.007.

Mattei, S., Tan, A., Glass, B., Müller, B., Kräusslich, H.-G., Briggs, J.A.G., 2018. High-resolution structures of HIV-1 Gag cleavage mutants determine structural switch for virus maturation. PNAS 115. https://doi.org/10.1073/pnas.1811237115.

Schorb, M., Haberbosch, I., Hagen, W.J.H., Schwab, Y., Mastronarde, D.N., 2019. Software tools for automated transmission electron microscopy. Nat. Methods 16, 471–477. https://doi.org/10.1038/s41592-019-0396-9.

Schur, F.K.M., Obr, M., Hagen, W.J.H., Wan, W., Jakobi, A.J., Kirkpatrick, J.M., Sachse, C., Kräusslich, H.-G., Briggs, J.A.G., 2016. An atomic model of HIV-1 capsid-SP1 reveals structures regulating assembly and maturation. Science 353, 506–508. https://doi.org/10.1126/science.aaf9620.

Schur, F.K.M., 2019. Toward high-resolution in situ structural biology with cryo-electron tomography and subtomogram averaging. Curr. Opin. Struct. Biol. 58, 1–9. https://doi.org/10.1016/j.sbi.2019.03.018.

Shikuma, N.J., Pilhofer, M., Weiss, G.L., Hadfield, M.G., Jensen, G.J., Newman, D.K., 2014. Marine tubeworm metamorphosis induced by arrays of bacterial phage tail-like structures. Science 343, 529–533. https://doi.org/10.1126/science.1246794.

Weiss, G.L., Medeiros, J.M., Pilhofer, M., 2017. In situ imaging of bacterial secretion systems by electron cryotomography. Methods Mol. Biol. 1615, 353–375. https://doi.org/10.1007/978-1-4939-7033-9_27.

Winkler, H., 2007. 3D reconstruction and processing of volumetric data in cryo-electron tomography. J. Struct. Biol. 157, 126–137. https://doi.org/10.1016/j.jsb.2006.07.014.

Xu, M., Singla, J., Tocheva, E.I., Chang, Y.-W., Stevens, R.C., Jensen, G.J., Alber, F., 2019. De novo structural pattern mining in cellular electron cryotomograms. Structure 27, 679–691. https://doi.org/10.1016/j.str.2019.01.005.

Zhang, K., 2016. Gctf: Real-time CTF determination and correction. J. Struct. Biol. 193, 1–12. https://doi.org/10.1016/j.jsb.2015.11.003.

Zheng, Q.S., Braunfeld, M.B., Sedat, J.W., Agard, D.A., 2004. An improved strategy for automated electron microscopic tomography. J. Struct. Biol. 147, 91–101. https://doi.org/10.1016/j.jsb.2004.02.005.

Ziese, U., Janssen, A.H., Murk, J.L., Geerts, W.J.C., Van der Krift, T., Verkleij, A.J., Koster, A.J., 2002. Automated high-throughput electron tomography by pre-calibration of image shifts. J. Microsc. 205, 187–200. https://doi.org/10.1046/j.0022-2720.2001.00987.x.